Wide distribution and partial melting of eclogite indicated by the X-discontinuity in the upper mantle

Jian Song[1], Wangsheng Qian[1], Shangqin Hao[1], Wenzhong Wang[2], Daoyuan Sun[1], and Zhongqing Wu[1]
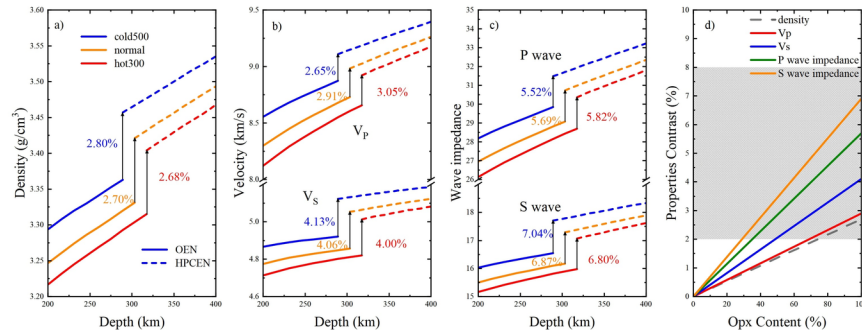
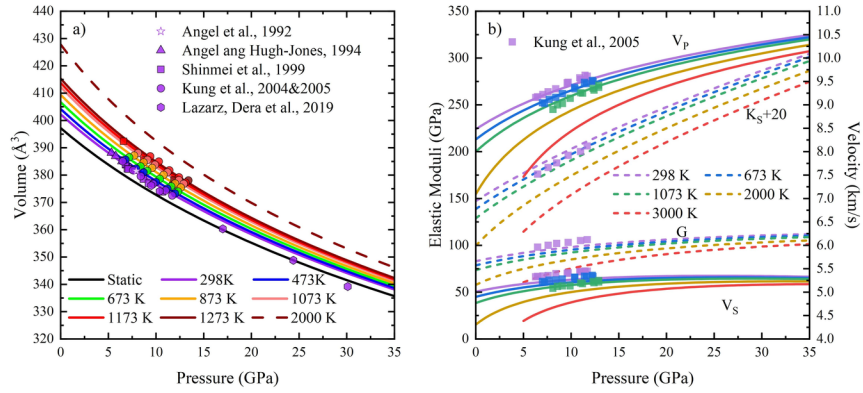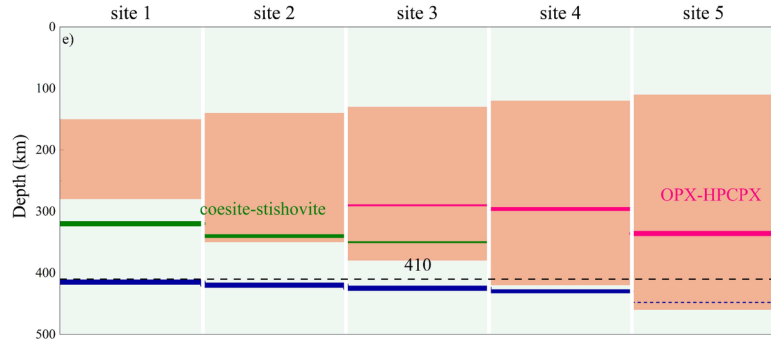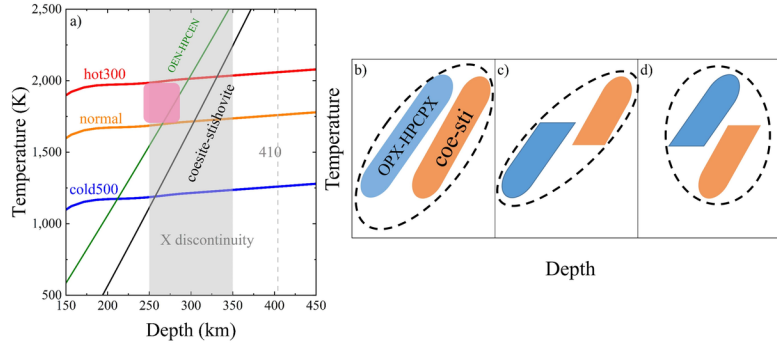[1]University of Science and Technology of China
[2]University College London

November 23, 2022

Abstract

Whether and where recycled oceanic crusts melt in the deep mantle are fundamentally important questions for understanding the evolution and dynamics of the Earth's mantle, and they currently remain unclear. Here, we find compelling evidence for the wide distribution of eclogite melting around a depth of 300 km by investigating the origins of the X-discontinuity. We show that both the transformation of orthopyroxene into high-pressure clinopyroxene and the coesite-stishovite transition are dominant mechanisms. The degree of partial melting of oceanic crust is crucial for the X-discontinuity mechanisms since melting promotes the enrichment of orthopyroxene by consuming solid silica. The silica phase transition dominates in the relatively low-temperature region, while the orthopyroxene phase transition in the high-temperature region results in the indistinguishable seismological Clapeyron slope of the X-discontinuity, with both transitions presenting a large positive Clapeyron slope. The X-discontinuity provides a key method for identifying partial melting of recycled oceanic crust.

1

a)

2,500

2,000 — hot300

1,500 — normal

— cold500

1,000

500

150 200 250 300 350 400 450

Temperature (K)

Depth (km)

OPX-HPCEN

coesite-stishovite

410

X discontinuity

b) OPX-HPCPX coe-sti

c)

d)

Temperature

Depth

site 1   site 2   site 3   site 4   site 5

e)

0

100

200

300

400

500

Depth (km)

coesite-stishovite

410

OPX-HPCPX

a)

440
430
420
410
400
390
380
370
360
350
340
330
320

Volume (Å³)

0   5   10   15   20   25   30   35

Pressure (GPa)

☆ Angel et al., 1992
△ Angel ang Hugh-Jones, 1994
■ Shinmei et al., 1999
● Kung et al., 2004&2005
● Lazarz, Dera et al., 2019

Static
673 K
1173 K
298K
873 K
1273 K
473K
1073 K
2000 K

b)

350

300

250

200

150

100

50

0

Elastic Moduli (GPa)

0   5   10   15   20   25   30   35

Pressure (GPa)

11.0
10.5
10.0
9.5
9.0
8.5
8.0
7.5
7.0
6.5
6.0
5.5
5.0
4.5
4.0

Velocity (km/s)

■ Kung et al., 2005

V_P

K_S+20

G

V_S

298 K   673 K
1073 K   2000 K
3000 K

1 **Wide distribution and partial melting of eclogite indicated by the X-**

2 **discontinuity in the upper mantle**

3 **Jian Song[1], Wangsheng Qian[1], Shangqin Hao[1], Wenzhong Wang[1,2,3], Daoyuan Sun[1,4],**

4 **Zhongqing Wu[1,4,5*]**

5 [1] Laboratory of Seismology and Physics of Earth's Interior, School of Earth and Space Sciences,

6 University of Science and Technology of China, Hefei 230026, China.

7 [2] Department of Earth Sciences, University College London, London WC1E 6BT, United

8 Kingdom.

9 [3] Earth and Planets Laboratory, Carnegie Institution for Science, Washington, DC 20015, USA.

10 [4] CAS Center for Excellence in Comparative Planetology, University of Science and Technology

11 of China, Hefei, Anhui, China.

12 [5] National Geophysical Observatory at Mengcheng, Anhui, China.

13 Corresponding author: Zhongqing Wu (wuzq10@ustc.edu.cn)

14 **Key Points:**

15 - The enrichment of 30% orthopyroxene is required to explain the X-discontinuity.

16 - Both the coesite-stishovite transition and the OPX-HPCPX transition are dominant
17   mechanisms for the genesis of the X-discontinuity.

18 - The X-discontinuity provides an effective approach to assess the melt situation of
19   eclogite in the deep earth.
20

21 **Abstract**

22 Whether and where recycled oceanic crusts melt in the deep mantle are fundamentally important
23 questions for understanding the evolution and dynamics of the Earth's mantle, and they currently
24 remain unclear. Here, we find compelling evidence for the wide distribution of eclogite melting
25 around a depth of 300 km by investigating the origins of the X-discontinuity. We show that both
26 the transformation of orthopyroxene into high-pressure clinopyroxene and the coesite-stishovite
27 transition are dominant mechanisms. The degree of partial melting of oceanic crust is crucial for
28 the X-discontinuity mechanisms since melting promotes the enrichment of orthopyroxene by
29 consuming solid silica. The silica phase transition dominates in the relatively low-temperature
30 region, while the orthopyroxene phase transition in the high-temperature region results in the
31 indistinguishable seismological Clapeyron slope of the X-discontinuity, with both transitions
32 presenting a large positive Clapeyron slope. The X-discontinuity provides a key method for
33 identifying partial melting of recycled oceanic crust.

34 **Plain Language Summary**

35 The genesis of the X-discontinuity, which is characterized by wide depth variations and
36 indistinguishable seismological Clapeyron slopes, is not well understood. The coesite-stishovite
37 transition has been proposed as the mechanism underlying the X-discontinuity; however, previous
38 seismic studies frequently excluded the transformation of orthopyroxene (OPX) to high-pressure
39 clinopyroxene (HPCPX) because of its small impedance contrasts. In this study, we performed
40 first-principle calculations to obtain the elasticity of high-pressure clinoenstatite at high pressure
41 and high temperature. Our results show that impedance contrasts caused by the OPX-HPCPX
42 transition are two times larger than previously thought and hence cannot be ignored. Furthermore,
43 we emphasize the role of eclogite melt and propose that both the coesite-stishovite transition and
44 OPX-HPCPX transition are dominant mechanisms for the X-discontinuity, with the former
45 dominating where eclogite is hard to melt and the latter dominating where partial melting of
46 eclogite occurs. Thermal state analysis and seismological observations support the important role
47 of the OPX-HPCPX transition in the X-discontinuity and wide distribution of partial melting of
48 eclogite. The new interpretation not only well explains the indistinguishable Clapeyron slope of
49 the X-discontinuity but also provides an approach for identifying partial melting of eclogite in the
50 deep earth.

51

1 Introduction

53 Seismic discontinuities with impedance contrasts of 2%~8% in depth ranges of 250
54 km~350 km were initially designated the X-discontinuity by Revenaugh and Jordan (1991), and
55 they have been detected beneath various tectonic settings, such as stable continents and hotspots
56 and near subduction zones (Bagley and Revenaugh, 2008; Arwen Deuss and Woodhouse, 2002;
57 Revenaugh and Jordan, 1991; Schmerr, 2015; Srinu et al., 2021). The origin for the X-discontinuity
58 is still debated. Several mechanisms have been proposed, including the formation of phase A
59 $(Mg_7Si_2O_8(OH)_6)$ (Revenaugh and Jordan, 1991), the reaction of forsterite and periclase to
60 anhydrous phase B $(5Mg_2SiO_4 + 4MgO \rightarrow Mg_{14}Si_5O_{24})$ (Ganguly and Frost, 2006), the phase
61 transition from coesite to stishovite (Chen et al., 2015; Williams and Revenaugh, 2005), and the
62 phase transition from orthopyroxene (OPX, $(Mg,Fe)SiO_3$) to high-pressure clinopyroxene
63 (HPCPX) (*Akashi et al.*, 2009; *Alan B. Woodland*, 1998). Phase A is only stable in the pressure

64 and temperature (PT) range of hydrated cold slabs (Kawamoto, 1996; A B Woodland et al., 1997),
65 indicating that the formation of phase A can only provide an explanation for the X-discontinuity
66 observed within cold subduction zones. The formation of anhydrous phase B requires the local
67 enrichment of periclase, which would consume OPX first before reacting with olivine to form
68 anhydrous phase B. The mechanisms for generating substantial amounts of periclase remain
69 unclear and need to be answered in further studies (Chen et al., 2015).

70 The phase transition from coesite to stishovite (Chen et al., 2015; Williams and Revenaugh,
71 2005) generates very large wave impedance contrasts, and only 4~8 wt% free silica is required to
72 cause the observed X-discontinuity. Although the pyrolite model consists of no free silica, the
73 subducted oceanic crust contains certain amounts of silica in both the MORB and sediment layers
74 (Trønnes, 2009). Therefore, the silica transition has become a popular mechanism to explain the
75 X-discontinuity. However, the large Clapeyron slope of the transition is inconsistent with
76 seismological studies indicating that a clear Clapeyron slope was not observed for the X-
77 discontinuity (A. Deuss and Woodhouse, 2004).

78 The phase transition from OPX to HPCPX, which was first proposed by Angel et al. (1992),
79 has been considered to explain the formation of the X-discontinuity (Akashi et al., 2009; Alan B.
80 Woodland, 1998). The transition is completed within 5 km intervals (Alan B. Woodland, 1998).
81 However, impedance contrasts of the transition under mantle conditions have had a serious impact
82 on previous results regarding the possibility of the OPX-HPCPX transition for the X-discontinuity,
83 and they remain unclear because of the lack of elasticity of HPCPX at high PT. Thus, high-quality
84 elastic data of HPCPX at high PT are necessary to quantitatively evaluate the relationship between
85 the OPX-HPCPX transition and the occurrence of X-discontinuities.

86 In this study, we investigated the elasticity of high-pressure clinoenstatite (HPCEN,
87 MgSiO$_3$), a Mg endmember of HPCPX, at high PT via first-principle calculations based on density
88 functional theory and combined it with the elasticity of orthoenstatite (OEN, MgSiO$_3$), a Mg
89 endmember of OPX (Qian et al., 2018), to obtain impedance contrasts caused by the OEN-HPCEN
90 transition. We discussed the contribution of the OPX-HPCPX transition to the genesis of the X-
91 discontinuity by considering the effect of eclogite melt on OPX enrichment.

92

2 Methods and calculation details

94 According to *Barron and Klein* (1965), isothermal elastic constants can be obtained by

$$c_{ijkl}^T = \frac{1}{V}\left(\frac{\partial^2 F}{\partial e_{ij}\partial e_{kl}}\right) + \frac{1}{2}P\big(2\delta_{ij}\delta_{kl} - \delta_{il}\delta_{kj} - \delta_{ik}\delta_{jl}\big) \tag{1}$$

96 where F and e_{ij} (i,j=1,2,3) represent the Helmholtz free energy and the infinitesimal strains,
97 respectively. In the quasi-harmonic approximation (QHA), F is expressed as

$$F\big(e_{ij},V,T\big) = U\big(e_{ij},V\big) + \frac{1}{2}\sum_{q,m}\hbar\omega_{q,m}\big(e_{ij},V\big) + k_B T\sum_{q,m}ln\left\{1 - exp\left[-\frac{\hbar\omega_{q,m}\big(e_{ij},V\big)}{k_B T}\right]\right\} \tag{2}$$

99 where T, V, K$_B$, and $\hbar$ represent the temperature, volume, Boltzmann and reduced Planck
100 constants, respectively; and ω and its subscripts q and m denote vibrational frequencies, the
101 phonon wave vector and the normal mode index. The first, second, and third terms on the right-
102 hand side of Eq. (2) are the static internal energy, zero-point energy, and vibrational energy

103   contributions at a given strain e_{ij} and volume V, respectively. Based on Eq. (1), to obtain thermal
104   elastic constants, the vibrational density of states (VDos) of many strained configurations must be
105   calculated using conventional methods, which are computationally expensive. *Wu and*
106   *Wentzcovitch* (2011) developed a semianalytical method where only the VDos of the unstrained
107   configuration is needed to obtain high-T elasticity, and this method has lowered the computational
108   workload to less than ten percent that of conventional methods. This method has been applied
109   successfully to MgO (*Wu and Wentzcovitch*, 2011), ringwoodite (*Valdez et al.*, 2012), olivine and
110   wadsleyite (*Núñez-Valdez et al.*, 2013), ferropericlase (*Wu et al.*, 2013), stishovite and $CaCl_2$-type
111   silica (*R Yang and Wu*, 2014), bridgmanite (*Shukla et al.*, 2015), pyrope (*Hu et al.*, 2016),
112   superhydrous phase B (*D P Yang et al.*, 2017), orthoenstatite (*Qian et al.*, 2018), diopside (*Zou et*
113   *al.*, 2018), corundum (*Wang and Wu*, 2018), magnesite (*Yao et al.*, 2018), and akimotoite (*Hao et*
114   *al.*, 2019). *Zou et al.* (2018) further generalized the method to monoclinic crystal systems.
115   Similarly, we use the developed method to calculate the elastic properties of HPCEN.

116   The open-source Quantum ESPERSSO package (*Giannozzi et al.*, 2009) based on density
117   functional theory was used to perform all calculations in this study. Local density approximation
118   (LDA) was chosen to handle the exchange correlation energy. The pseudopotentials for oxygen
119   and silicon were generated by the norm-conserving Troullier-Martins method (*Troullier and*
120   *Martins*, 1991). The pseudopotential for magnesium was generated by the method of von Barth
121   and Car (*Karki et al.*, 2000). The crystal structure was optimized by the variable cell-shape damped
122   molecular dynamic method (*Wentzcovitch*, 1991), and the dynamical matrices were calculated
123   based on density-functional perturbation theory (*Baroni et al.*, 2001) with a $2 \times 2 \times 2$ q-point
124   mesh. The cutoff energy of plane wave expansion was 70 Ry. Elastic constants in static conditions
125   were calculated according to the stress-strain relationship, and 1% strain was imposed.

126   **3 Results**

127   **3.1 Equation of states of HPCEN**

128   The calculated equation of states of HPCEN ($MgSiO_3$) is consistent with the available
129   experimental results up to the highest measured temperature of 1273 K (Fig. 1a and Table S1-S2)
130   (Angel and Hugh-Jones, 1994; Angel et al., 1992; J. Kung et al., 2005; Jennifer Kung et al., 2004;
131   Lazarz et al., 2019; Li et al., 2014; Shinmei et al., 1999; Yu and Wentzcovitch, 2009). The
132   differences between the calculated and experimental volumes are less than 0.5% for almost all
133   experimental results except for those of Lazarz et al. (2019), which gradually deviated from the
134   calculated results to a value of 1.42% at 30 GPa with increasing pressure.

135

136   **3.2 Elasticity of HPCEN at high PT**

137   With space Group C2/c, the elastic tensor of HPCEN is fully determined by thirteen
138   independent single-crystal elastic constants C_{11}, C_{22}, C_{33}, C_{12}, C_{13}, C_{23}, C_{44}, C_{55}, C_{66}, C_{15}, C_{25}, C_{35},
139   and C_{46}. Experimental data for elastic constants are still not available. Li et al. (2014) provided
140   static GGA results, and after pressure correction, their results match our LDA static results very
141   well (Fig. S1 and Table S3).

142   The adiabatic bulk modulus (K_S) and shear modulus (G) were obtained via the Voigt-
143 Reuss-Hill averaging method (Hill, 1952). The calculated K_S and G of HPCEN are consistent with
144 ultrasonic measurements (Fig. 1b). Both K_S and G have nonlinear relationships with pressure in
145 the range of 0-35 GPa, especially for G. For example, at ambient temperature, $\frac{\partial Ks}{\partial P}$ and $\frac{\partial G}{\partial P}$ change
146 from 6.53 and 2.14 at 0 GPa to 4.89 and 1.06 at 10 GPa, respectively. The compressional wave
147 velocity (V_P) and shear wave velocity (V_S) can be derived from the density and elastic moduli K_S

148 and G as $V_P = \sqrt{\dfrac{K_S + \frac{4}{3}G}{\rho}}, V_S = \sqrt{\dfrac{G}{\rho}}$. The calculated results are well in line with the results of J.

149 Kung et al. (2005) for V_P, regardless of temperature, whereas there are some discrepancies for V_S,
150 with a maximum of ~2-2.5% at ambient temperature and gradual shrinkage with increasing
151 temperature (Fig. 1b). The fitting parameters of elastic moduli and velocities as a function of
152 pressure and temperature are reported in Table S4.

3.3 Property contrasts caused by the OEN-HPCEN transition

154   Combined with the elasticity of the OEN at high PT from Qian et al. (2018), we evaluated
155 the property contrast caused by the OEN-HPCEN transformation expressed as $\delta M =$
156 $\frac{2 \times (M_{HPCEN} - M_{OEN})}{M_{HPCEN} + M_{OEN}} \times 100\%$, where M denotes different properties, including density, V_P, V_S, P
157 wave impedance, and S wave impedance. At room temperature, OEN transforms into HPCEN with
158 ~2.7%, ~2.9%, and ~4.1% jumps for density, V_P, and V_S, respectively, which is consistent with
159 the results of Jennifer Kung et al. (2004). The OPX-HPCPX transition should have similar
160 impedance contrasts due to the similar Fe partitioning behavior between OPX and HPCPX (A
161 Woodland et al., 1997). Under the PT conditions of the X-discontinuity, the transition accompanies
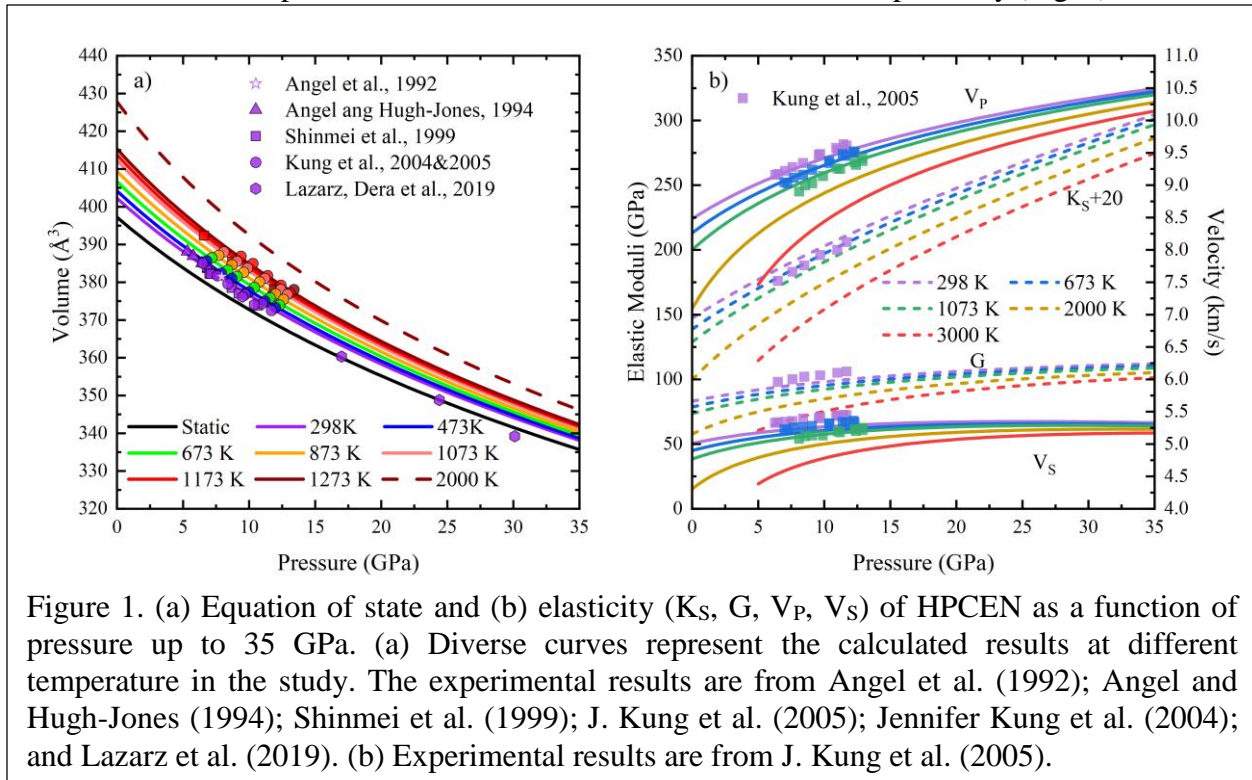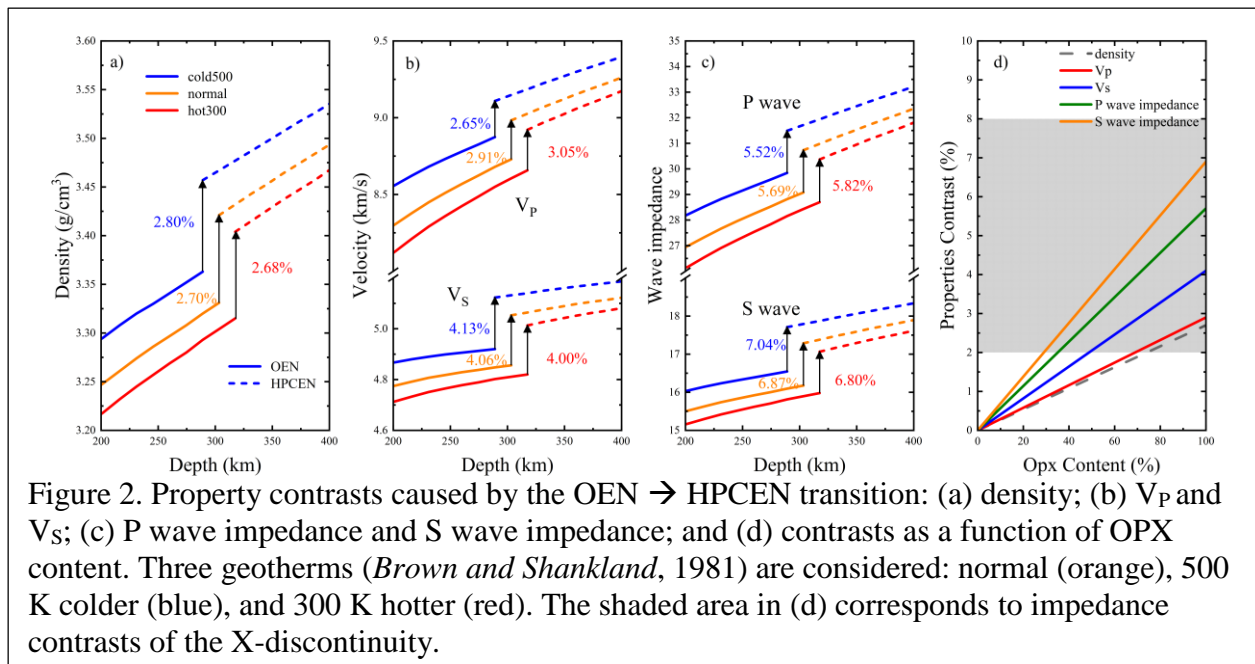162 ~5.7% and ~6.9% impedance contrasts for the P wave and S wave, respectively (Fig. 2). In addition,

Figure 1. (a) Equation of state and (b) elasticity (K_S, G, V_P, V_S) of HPCEN as a function of pressure up to 35 GPa. (a) Diverse curves represent the calculated results at different temperature in the study. The experimental results are from Angel et al. (1992); Angel and Hugh-Jones (1994); Shinmei et al. (1999); J. Kung et al. (2005); Jennifer Kung et al. (2004); and Lazarz et al. (2019). (b) Experimental results are from J. Kung et al. (2005).

163 20% OPX corresponds to 1.2% P wave and 1.4% S wave impedance contrasts. These values are
164 two times larger than those of Alan B Woodland and Angel (1997), which were assumed from
165 Birch's law without direct wave speed measurements. Since Kemp et al. (2019) and Pugh et al.
166 (2021) adopted underestimated impedance contrasts of Alan B Woodland and Angel (1997), they
167 inappropriately ruled out the OPX-HPCPX transition in advance. According to our results, the
168 OPX-HPCPX transition has the ability to generate seismically detected X-discontinuities as long
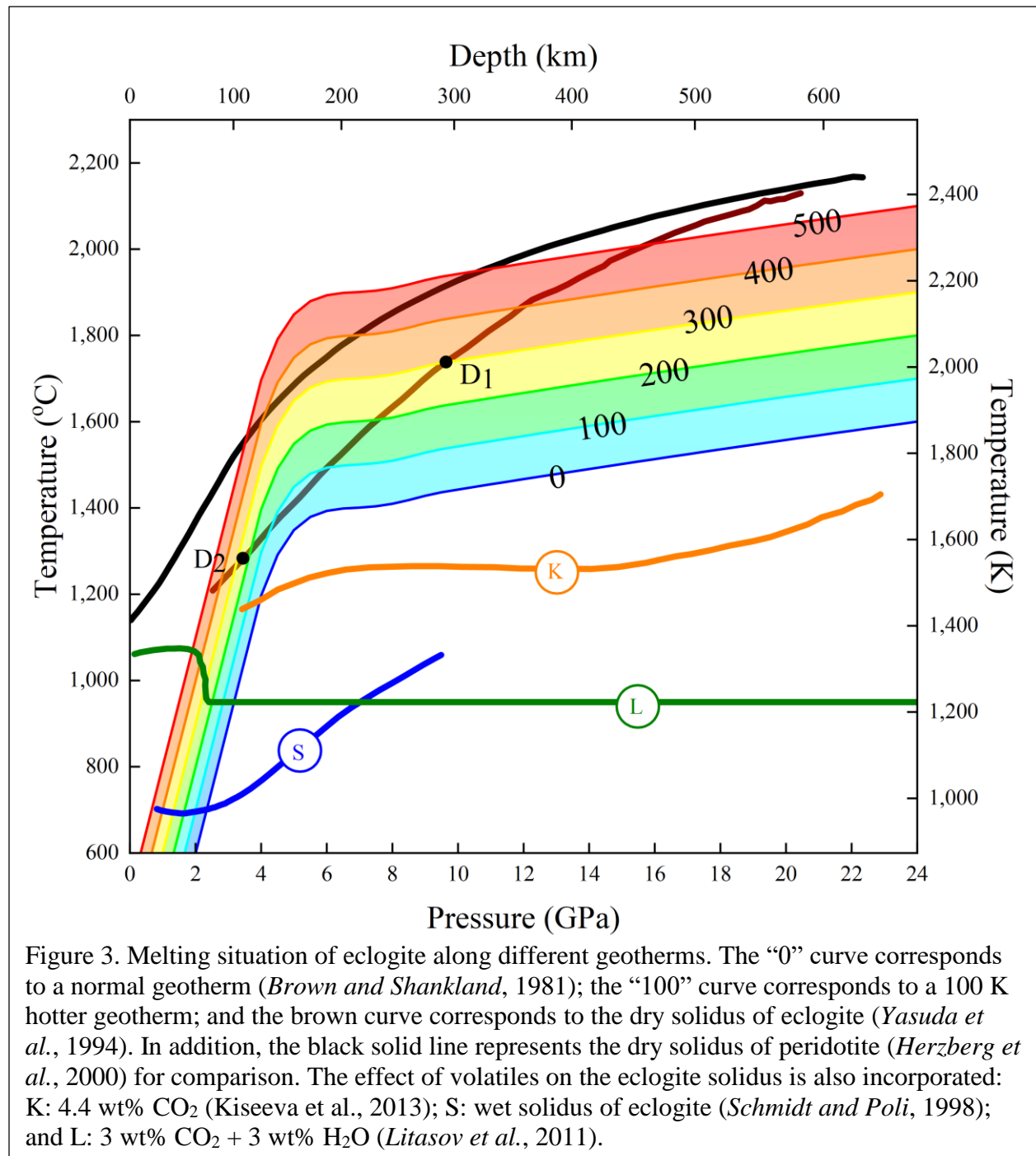169 as the OPX content exceeds 30% (Fig. 2d).

170 **4. Discussion**

171 **4.1 OPX enrichment and partial melting of eclogite**

172   OPX is an important major mineral in the upper mantle, occupying ~10% of the pyrolite
173 model and gradually dissolving into garnet. Therefore, the OPX in the pyrolite model is
174 insufficient to generate visible X-discontinuities (Frost, 2008), and greater amount of OPX is
175 required for the formation of the X-discontinuity. Within subduction zones, the harzburgite layer,
176 which is the mantle residual part after MORB extraction, is more depleted and contains ~13%
177 OPX on average (Matsukage et al., 2005). In addition, the enrichment of OPX is mainly achieved
178 by melt/rock reactions between silica-rich melts generally derived from eclogite and surrounding
179 peridotite at the expense of olivine. Although experimental studies have widely demonstrated the
180 OPX-enrichment mechanism (Gervasoni et al., 2017; Mallik and Dasgupta, 2012; Rapp et al., 1999;
181 Yaxley and Green, 1998), whether eclogite melts around the depth range of the X-discontinuity,

Figure 2. Property contrasts caused by the OEN → HPCEN transition: (a) density; (b) V_P and V_S; (c) P wave impedance and S wave impedance; and (d) contrasts as a function of OPX content. Three geotherms (*Brown and Shankland*, 1981) are considered: normal (orange), 500 K colder (blue), and 300 K hotter (red). The shaded area in (d) corresponds to impedance contrasts of the X-discontinuity.

182 which has comprehensive implications for the processes of Earth's interior, remains uncertain.
183 Here, we show compelling evidence for the OPX-HPCPX transition as one of the dominant
184 mechanisms of the X-discontinuity and the wide distribution of melting of eclogite around the
185 depth range of the X-discontinuity.

186   The estimates of the melting situation of eclogite based on a volatile-free dry solidus of
187 eclogite (Yasuda et al., 1994) and a relatively low geotherm (Brown and Shankland, 1981) are
188 conservative compared to that using other reported geotherms (Katsura et al., 2010). The

Figure 3. Melting situation of eclogite along different geotherms. The "0" curve corresponds
to a normal geotherm (*Brown and Shankland*, 1981); the "100" curve corresponds to a 100 K
hotter geotherm; and the brown curve corresponds to the dry solidus of eclogite (*Yasuda et
al.*, 1994). In addition, the black solid line represents the dry solidus of peridotite (*Herzberg et
al.*, 2000) for comparison. The effect of volatiles on the eclogite solidus is also incorporated:
K: 4.4 wt% CO_2 (Kiseeva et al., 2013); S: wet solidus of eclogite (*Schmidt and Poli*, 1998);
and L: 3 wt% CO_2 + 3 wt% H_2O (*Litasov et al.*, 2011).

189 estimations clearly suggest that eclogite is subject to partial melting in high-temperature regions.
190 Taking eclogite entrained by the upwelling plume as an example, it starts to melt at depth D_1 and
191 then crystallizes at shallower depth D_2 ($D_1 > D_2$) along the hot geotherm. As shown in Fig. 3, the
192 depth interval where eclogite will partially melt (D_1, D_2) broadens quickly with increasing
193 temperature. D_1 approaches 300 km, and OPX can be locally enriched at a depth of 300 km under
194 300 K hotter conditions. When the geotherm is 500 K hotter, eclogite starts to melt at a depth of
195 ~450 km and has a larger melting degree at 300 km, suggesting that there is less solid-state silica
196 but more OPX enrichment. Thus, OPX enrichment is likely to be achieved in hot regions. The
197 presence of H_2O or CO_2 dramatically decreases the solidus of eclogite (Kiseeva et al., 2013;
198 Litasov et al., 2011; Schmidt and Poli, 1998) (Fig. 3) and further promotes the partial melting of
199 volatile-bearing recycled oceanic crust. Thus, the OPX-HPCPX transition likely plays an
200 important role in the origin of the X-discontinuity in hot or wet areas.

4.2 Seismological support

202   Although precisely determining the mechanism underlying the observed X-discontinuity
203 is difficult, there are indeed some special seismological signals to help us discriminate the origin
204 of the X-discontinuity. We noted that several recent seismological studies on the X-discontinuity
205 (Kemp et al., 2019; Pugh et al., 2021; Rein et al., 2020) support our view.

4.2.1 X-discontinuity and disappearance of 410 beneath the Hawaii hotspot

207   Kemp et al. (2019) found that the X-discontinuity, with an average depth of 296 km, exists
208 throughout the entire area beneath Hawaii. The X-discontinuity becomes deeper and stronger,
209 while the 410 discontinuity becomes deeper but weaker and even vanishes in the eastern part of
210 the Big Island. Kemp et al. (2019) simply excluded the OPX-HPCPX transition based on the results
211 of Alan B Woodland and Angel (1997) and proposed that the X-discontinuity results from the
212 coesite-stishovite transition in eclogite. In fact, our calculation shows that the OPX-HPCPX
213 transition can cause X-discontinuities with a large impedance contrast (Fig. 2d). Moreover, the
214 coesite-stishovite transition for the X-discontinuity beneath Hawaii (Kemp et al., 2019) faces
215 several fundamental challenges. As shown in Fig. 4a, the depth of the X-discontinuity (~300 km)
216 is significantly shallower than the coesite-stishovite transition considering the high temperature
217 beneath the Hawaii hotspot. Furthermore, the deeper depths of the X-discontinuity and 410 in the
218 eastern part of Big Island (Kemp et al., 2019) indicate that the eastern part has a higher temperature
219 and larger melting degree of eclogite than other areas, which means a weaker X-discontinuity
220 signal. This finding conflicts with the observed stronger X-discontinuity signal in the eastern part.
221 Finally, an accumulation of eclogite >60%, which is required to explain the disappearance of 410
222 according to synthesis tests (Kemp et al., 2019), will be >3% denser than ambient mantle and
223 generate gravitational instability (*Maxim D Ballmer et al.*, 2015; *Maxim D. Ballmer et al.*, 2013).
224 In contrast, these challenges become strong arguments for the X-discontinuity resulting from the
225 OPX-HPCPX transition. Beneath Hawaii, Si-rich melts derived from eclogite carried by the
226 upwelling plume react with surrounding peridotite to enrich OPX at the expense of olivine. The
227 OPX-HPCPX transition, which occurs at a much shallower depth than the coesite-stishovite
228 transition (Fig. 4a), is consistent with the depth of the X-discontinuity. A larger degree of melting,
229 which means a larger degree of enrichment of OPX and consumption of olivine, can well explain
230 the stronger X-discontinuity and the weaker and even vanished 410 in the hotter east part. High-
231 Ni and high-Si parental Hawaiian magmas also indicate that their source is not peridotite but
232 olivine-free pyroxenite formed by consuming olivine (Sobolev et al., 2005; Sobolev et al., 2007).

4.2.2 Double X-discontinuities beneath Southwest Morocco

The X-discontinuity beneath Southwest Morocco (SW Morocco) (Rein et al., 2020) provides more cogent evidence on the important role of the OPX-HPCPX transition in the X-discontinuity. According to local tectonic settings and the relationship between temperature and lithospheric thickness, Rein et al. (2020) found that the temperature in the study area rises successively from the west, southeast, and northeast regions. Receiver function results show that from west to southeast, the X-discontinuity signal weakens and the depth of the X-discontinuity increases from 310~340 km to 330~350 km. The situation is the most complicated in the northeast. Double weak X-discontinuities are detected, with one at 285~295 km and the other at 330~350 km. In the northernmost part, the deeper part disappears, leaving the shallow part untouched (see Figure 5 in Rein et al. (2020)). The scenario is completely consistent with our point of view. The free solid-state silica is preserved to the largest extent and generates the strongest X-discontinuity in the coldest west. The higher temperature in the southeast results in a deeper X-discontinuity because of the positive Clapeyron slope of the silica transition and weaker signal because more eclogite melts to reduce solid-state silica. Although the melting of silica promotes the enrichment of OPX, the OPX in the southeast is still less than 30%, and its phase transition cannot produce a detectable discontinuity. With further increases in temperature in the northeast, the enrichment of OPX is eventually enough to be detected and results in relatively weak double X-discontinuities, which are shallower for the OPX-HPCPX transition and deeper for the coesite-stishovite transition. With higher temperatures, silica-induced X-discontinuities cannot be detected and OPX-induced X-discontinuities become stronger, corresponding to the single 290-km X-discontinuity in the northernmost part. Such double X-discontinuities demonstrate that the OPX-HPCPX transition can indeed cause X-discontinuities in hot areas.

By combining these studies together, we found further evidence to support our view on the cause of the X-discontinuity beneath Hawaii. It is acceptable that the Hawaii hotspot should be hotter than SW Morocco, which is also supported by seismological results: the 410 in Hawaii depresses by ~20 km (Kemp et al., 2019) while the 410 in SW Morocco depresses by only ~10 km (Lawrence and Shearer, 2006; Spieker et al., 2014). If the X-discontinuity beneath Hawaii is caused by a silica phase transition, it should be deeper than the X-discontinuity associated with the silica transition beneath SW Morocco due to the strong positive Clapeyron slope of the coesite-stishovite transition. However, the average depth of the Hawaiian X-discontinuity (296 km) is significantly shallower than those of even the coldest part of SW Morocco (310~330 km). Similarly, all robust X-discontinuities beneath 15 hotspots except Tahiti reported by Pugh et al. (2021) occur at depths less than 280 km (pink area in Fig. 4a) and thus should also result from the OPX-HPCPX transition rather than the coesite-stishovite transition suggested by Pugh et al. (2021).
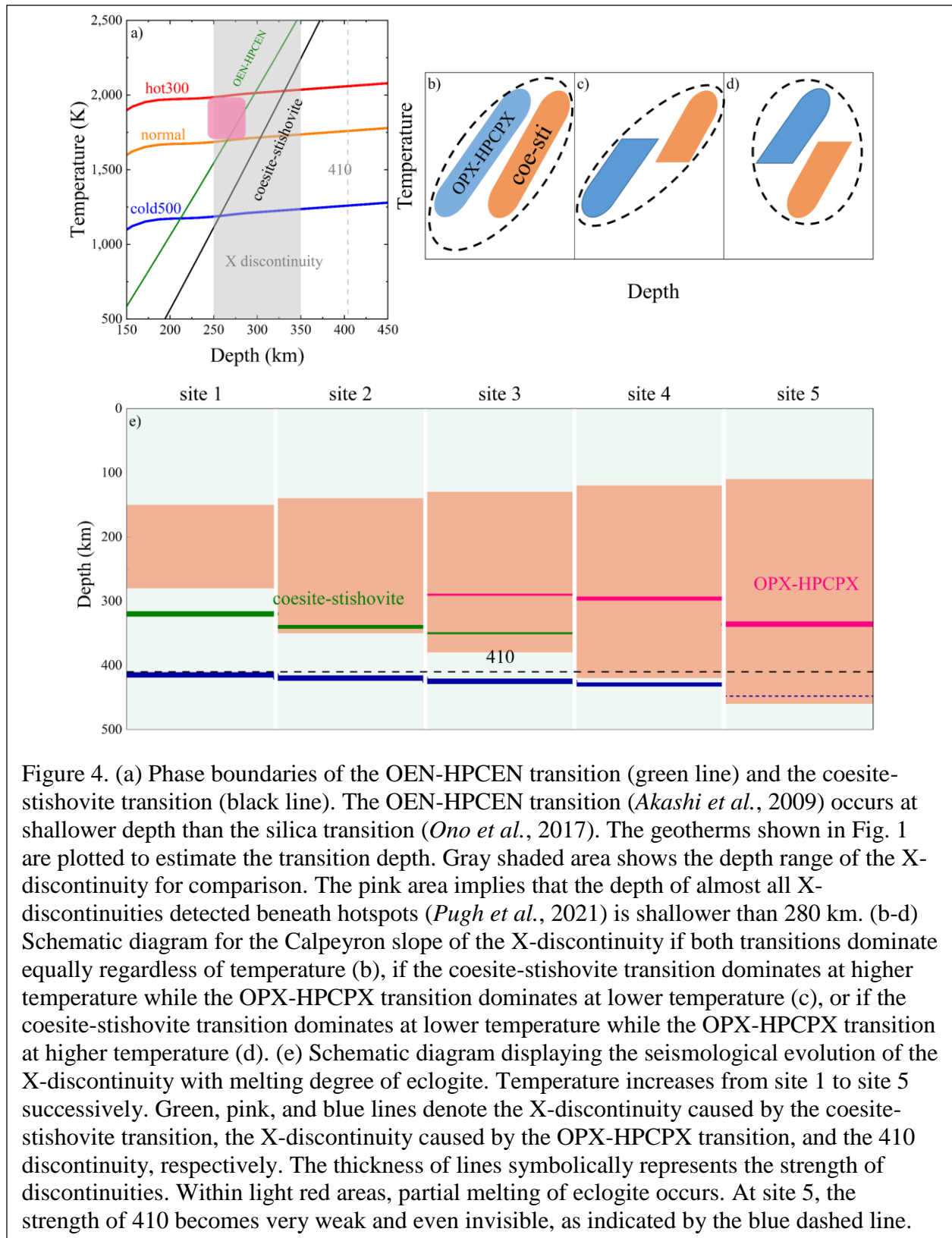
Figure 4. (a) Phase boundaries of the OEN-HPCEN transition (green line) and the coesite-stishovite transition (black line). The OEN-HPCEN transition (*Akashi et al.*, 2009) occurs at shallower depth than the silica transition (*Ono et al.*, 2017). The geotherms shown in Fig. 1 are plotted to estimate the transition depth. Gray shaded area shows the depth range of the X-discontinuity for comparison. The pink area implies that the depth of almost all X-discontinuities detected beneath hotspots (*Pugh et al.*, 2021) is shallower than 280 km. (b-d) Schematic diagram for the Calpeyron slope of the X-discontinuity if both transitions dominate equally regardless of temperature (b), if the coesite-stishovite transition dominates at higher temperature while the OPX-HPCPX transition dominates at lower temperature (c), or if the coesite-stishovite transition dominates at lower temperature while the OPX-HPCPX transition at higher temperature (d). (e) Schematic diagram displaying the seismological evolution of the X-discontinuity with melting degree of eclogite. Temperature increases from site 1 to site 5 successively. Green, pink, and blue lines denote the X-discontinuity caused by the coesite-stishovite transition, the X-discontinuity caused by the OPX-HPCPX transition, and the 410 discontinuity, respectively. The thickness of lines symbolically represents the strength of discontinuities. Within light red areas, partial melting of eclogite occurs. At site 5, the strength of 410 becomes very weak and even invisible, as indicated by the blue dashed line.

270

4.3 Evolution of the X-discontinuity with the melting degree of eclogite

The X-discontinuity beneath SW Morocco and hotspots actually well represent the variations in the X-discontinuity with the melting degree of eclogite (Fig. 4e). Site 1 in Fig. 4e, which indicates the western part of SW Morocco, has temperatures close to the normal mantle, and there is enough solid-state silica to produce strong X-discontinuities. At site 2, eclogite melts at depths deeper than 300 km but the OPX enrichment is not enough to produce detectable discontinuities. In this case, one weaker but deeper X-discontinuity is observed in the seismology that represents the southeastern part of SW Morocco. At site 3, a larger melting degree leads to OPX enrichment that exceeds 30%. The relevant X-discontinuity can be detected, while the silica-induced X-discontinuity can still be observed, although its strength diminishes, resulting in double X-discontinuity, as found beneath the northeastern part of SW Morocco (Rein et al., 2020) and the following hotspots: Marquesas, Samoa, and St. Helena (Pugh et al., 2021). When temperatures continue to increase at site 4, which is also observed at the hottest part in SW Morocco (Rein et al., 2020), at most hotspots (Pugh et al., 2021), and at the Hawaii site investigated by Kemp et al. (2019) except for the eastern part of Big Island, the silica-relevant X-discontinuity eventually disappears while the OPX-related X-discontinuity becomes stronger. Thus, there is only one shallow X-discontinuity appearing in the seismology results. When the temperature increases to a certain degree, olivine near the 410 discontinuity is also consumed by the eclogite melt and the strength of the 410 is thus affected more or less and even disappears, as shown at site 5 (represented by the eastern Big Island (Kemp et al., 2019)).

4.4 Indistinguishable seismological Clapeyron slope of the X-discontinuity

Among the mechanisms causing the X-discontinuity, the OPX-HPCPX transition and the coesite-stishovite transition are the most plausible. Partial melting of eclogite is crucial for both mechanisms since it promotes the enrichment of OPX by reducing the solid-state silica content. In relatively low-temperature and volatile-poor regions, where eclogite is hard to melt, the coesite-stishovite transition is dominant. In contrast, in regions where a large degree of partial melting of eclogite occurs, the OPX-HPCPX transition is dominant. The interpretation of the genesis of the X-discontinuity is also supported by the indistinguishable seismological Clapeyron slope of the X-discontinuity (A. Deuss and Woodhouse, 2004). Their findings indicate that a single mineralogical mechanism is insufficient since these transitions have a large positive Clapeyron slope. If both transitions dominate equally regardless of temperature (Fig. 4b) or if the coesite-stishovite transition dominates at higher temperatures while the OPX-HPCPX transition dominates at lower temperatures (Fig. 4c), then an obviously positive Clapeyron slope will be detected. In contrast, when the coesite-stishovite transition dominates at lower temperatures while the OPX-HPCPX transition dominates at higher temperatures (Fig. 4d), there is no strong relationship between temperature and depth, which naturally provides an explanation for the indistinguishable seismological Clapeyron slope of the X-discontinuity (A. Deuss and Woodhouse, 2004). Consequently, the dominance of the OPX-HPCPX transition together with the coesite-stishovite transition for the X-discontinuity suggests ubiquity of partial melting of recycled oceanic crust around a depth of 300 km. The X-discontinuity provides a key method of identifying partial melting of recycled oceanic crust.

314 **Acknowledgments**

319 **Data Availability Statement**

320   The authors comply with the AGU's data policy, and the datasets in this paper are available
321 on zenodo via https://doi.org/10.5281/zenodo.5515367

322

323 **References**

324 Akashi, A., Y. Nishihara, E. Takahashi, Y. Nakajima, Y. Tange, and K. i. Funakoshi (2009),
325   Orthoenstatite/clinoenstatite phase transformation in MgSiO3at high‐pressure and high‐temperature determined
326   by in situ X‐ray diffraction: Implications for nature of the X discontinuity, Journal of Geophysical Research,
327   114(B4). doi:10.1029/2008jb005894
328 Angel, R. J., and D. A. Hugh-Jones (1994), Equations of state and thermodynamic properties of enstatite pyroxenes,
329   Journal of Geophysical Research: Solid Earth, 99(B10), 19777-19783. doi:10.1029/94jb01750
330 Angel, R. J., A. Chopelas, and N. L. Ross (1992), Stability of high-density clinoenstatite at upper-mantle pressures,
331   Nature, 358(6384), 322-324. doi:DOI 10.1038/358322a0
332 Bagley, B., and J. Revenaugh (2008), Upper mantle seismic shear discontinuities of the Pacific, Journal of
333   Geophysical Research-Solid Earth, 113(B12). doi:10.1029/2008jb005692
334 Ballmer, M. D., G. Ito, and C. Cheng (2015), Asymmetric dynamical behavior of thermochemical plumes and
335   implications for Hawaiian lava composition, Hawaiian Volcanoes: From Source to Surface, 208, 35
336 Ballmer, M. D., G. Ito, C. J. Wolfe, and S. C. Solomon (2013), Double layering of a thermochemical plume in the
337   upper mantle beneath Hawaii, Earth and Planetary Science Letters, 376, 155-164. doi:10.1016/j.epsl.2013.06.022
338 Baroni, S., S. de Gironcoli, A. Dal Corso, and P. Giannozzi (2001), Phonons and related crystal properties from
339   density-functional perturbation theory, Rev Mod Phys, 73(2), 515-562. doi:DOI 10.1103/RevModPhys.73.515
340 Barron, T., and M. Klein (1965), Second-order elastic constants of a solid under stress, Proceedings of the Physical
341   Society, 85(3), 523
342 Brown, J. M., and T. J. Shankland (1981), Thermodynamic parameters in the Earth as determined from seismic
343   profiles, Geophysical Journal International, 66(3), 579-596. doi:10.1111/j.1365-246X.1981.tb04891.x
344 Chen, T., G. D. Gwanmesia, X. Wang, Y. Zou, R. C. Liebermann, C. Michaut, and B. Li (2015), Anomalous elastic
345   properties of coesite at high pressure and implications for the upper mantle X-discontinuity, Earth and Planetary
346   Science Letters, 412, 42-51. doi:10.1016/j.epsl.2014.12.025
347 Deuss, A., and J. H. Woodhouse (2002), A systematic search for mantle discontinuities using SS-precursors,
348   Geophysical Research Letters, 29(8), 90-91-90-94. doi:10.1029/2002gl014768
349 Deuss, A., and J. Woodhouse (2004), The nature of the Lehmann discontinuity from its seismological Clapeyron
350   slopes, Earth and Planetary Science Letters, 225(3-4), 295-304. doi:10.1016/j.epsl.2004.06.021
351 Frost, D. J. (2008), The Upper Mantle and Transition Zone, Elements, 4(3), 171-
352   176. doi:10.2113/gselements.4.3.171
353 Ganguly, J., and D. J. Frost (2006), Stability of anhydrous phase B: Experimental studies and implications for phase
354   relations in subducting slab and the X discontinuity in the mantle, Journal of Geophysical Research: Solid Earth,
355   111(B6), n/a-n/a. doi:10.1029/2005jb003910
356 Gervasoni, F., S. Klemme, A. Rohrbach, T. Grützner, and J. Berndt (2017), Experimental constraints on mantle
357   metasomatism caused by silicate and carbonate melts, Lithos, 282, 173-186
358 Giannozzi, P., et al. (2009), QUANTUM ESPRESSO: a modular and open-source software project for quantum
359   simulations of materials, Journal of Physics: Condensed Matter, 21(39), 395502
360 Hao, S., W. Wang, W. Qian, and Z. Wu (2019), Elasticity of akimotoite under the mantle conditions: Implications
361   for multiple discontinuities and seismic anisotropies at the depth of ∼600–750 km in subduction zones, Earth and
362   Planetary Science Letters, 528. doi:10.1016/j.epsl.2019.115830

363 Herzberg, C., P. Raterron, and J. Zhang (2000), New experimental observations on the anhydrous solidus for
364   peridotite KLB-1, Geochemistry, Geophysics, Geosystems, 1(11). doi:10.1029/2000GC000089
365 Hill, R. (1952), The elastic behaviour of a crystalline aggregate, Proceedings of the Physical Society. Section A,
366   65(5), 349
367 Hu, Y., Z. Wu, P. K. Dera, and C. R. Bina (2016), Thermodynamic and elastic properties of pyrope at high pressure
368   and high temperature by first-principles calculations, Journal of Geophysical Research: Solid Earth, 121(9), 6462-
369   6476. doi:10.1002/2016jb013026
370 Karki, B. B., R. M. Wentzcovitch, S. de Gironcoli, and S. Baroni (2000), High-pressure lattice dynamics and
371   thermoelasticity of MgO, Physical Review B, 61(13), 8793-8800. doi:10.1103/PhysRevB.61.8793
372 Katsura, T., A. Yoneda, D. Yamazaki, T. Yoshino, and E. Ito (2010), Adiabatic temperature profile in the mantle,
373   Physics of the Earth and Planetary Interiors, 183(1-2), 212-218. doi:10.1016/j.pepi.2010.07.001
374 Kawamoto, T. (1996), Experimental evidence for a hydrous transition zone in the early Earth's mantle, Earth and
375   Planetary Science Letters, 142(3-4), 587-592. doi:10.1016/0012-821x(96)00113-6
376 Kemp, M., J. Jenkins, J. Maclennan, and S. Cottaar (2019), X-discontinuity and transition zone structure beneath
377   Hawaii suggests a heterogeneous plume, Earth and Planetary Science Letters, 527. doi:10.1016/j.epsl.2019.115781
378 Kiseeva, E. S., K. D. Litasov, G. M. Yaxley, E. Ohtani, and V. S. Kamenetsky (2013), Melting and Phase Relations
379   of Carbonated Eclogite at 9-21 GPa and the Petrogenesis of Alkali-Rich Melts in the Deep Mantle, Journal of
380   Petrology, 54(8), 1555-1583. doi:10.1093/petrology/egt023
381 Kung, J., B. S. Li, T. Uchida, and Y. B. Wang (2005), In-situ elasticity measurement for the unquenchable high-
382   pressure clinopyroxene phase: Implication for the upper mantle, Geophysical Research Letters, 32(1). doi:Artn
383   L01307
384 10.1029/2004gl021661
385 Kung, J., B. Li, T. Uchida, Y. Wang, D. Neuville, and R. C. Liebermann (2004), In situ measurements of sound
386   velocities and densities across the orthopyroxene → high-pressure clinopyroxene transition in MgSiO3 at high
387   pressure, Physics of the Earth and Planetary Interiors, 147(1), 27-44. doi:10.1016/j.pepi.2004.05.008
388 Lawrence, J. F., and P. M. Shearer (2006), A global study of transition zone thickness using receiver functions,
389   Journal of Geophysical Research: Solid Earth, 111(B6), n/a-n/a. doi:10.1029/2005jb003973
390 Lazarz, J. D., P. Dera, Y. Hu, Y. Meng, C. R. Bina, and S. D. Jacobsen (2019), High-pressure phase transitions of
391   clinoenstatite, American Mineralogist, 104(6), 897-904. doi:10.2138/am-2019-6740
392 Li, B., J. Kung, W. Liu, and R. C. Liebermann (2014), Phase transition and elasticity of enstatite under pressure
393   from experiments and first-principles studies, Physics of the Earth and Planetary Interiors, 228, 63-
394   74. doi:10.1016/j.pepi.2013.11.009
395 Litasov, K. D., A. F. Shatskiy, and N. P. Pokhilenko (2011), Phase relations and melting in the systems of
396   peridotite-H2O-CO2 and eclogite-H2O-CO2 at pressures up to 27 GPa, Doklady Earth Sciences, 437(2), 498-
397   502. doi:10.1134/s1028334x11040143
398 Mallik, A., and R. Dasgupta (2012), Reaction between MORB-eclogite derived melts and fertile peridotite and
399   generation of ocean island basalts, Earth and Planetary Science Letters, 329-330, 97-
400   108. doi:10.1016/j.epsl.2012.02.007
401 Matsukage, K. N., Y. Nishihara, and S.-i. Karato (2005), Seismological signature of chemical differentiation of
402   Earth's upper mantle, Journal of Geophysical Research, 110(B12). doi:10.1029/2004jb003504
403 Núñez-Valdez, M., Z. Wu, Y. G. Yu, and R. M. Wentzcovitch (2013), Thermal elasticity of
404   (Fex,Mg1−x)2SiO4olivine and wadsleyite, Geophysical Research Letters, 40(2), 290-294. doi:10.1002/grl.50131
405 Ono, S., T. Kikegawa, Y. Higo, and Y. Tange (2017), Precise determination of the phase boundary between coesite
406   and stishovite in SiO2, Physics of the Earth and Planetary Interiors, 264, 1-6. doi:10.1016/j.pepi.2017.01.003
407 Pugh, S., J. Jenkins, A. Boyce, and S. Cottaar (2021), Global receiver function observations of the X-discontinuity
408   reveal recycled basalt beneath hotspots, Earth and Planetary Science Letters, 561. doi:10.1016/j.epsl.2021.116813
409 Qian, W., W. Wang, F. Zou, and Z. Wu (2018), Elasticity of Orthoenstatite at High Pressure and Temperature:
410   Implications for the Origin of Low V_P/V_S Zones in the Mantle Wedge, Geophysical Research Letters, 45(2),
411   665-673. doi:10.1002/2017gl075647
412 Rapp, R. P., N. Shimizu, M. D. Norman, and G. S. Applegate (1999), Reaction between slab-derived melts and
413   peridotite in the mantle wedge: experimental constraints at 3.8 GPa, Chemical Geology, 160(4), 335-
414   356. doi:10.1016/s0009-2541(99)00106-0
415 Rein, T., K. Hannemann, C. Thomas, and M. Korn (2020), Location and characteristics of the X-discontinuity
416   beneath SW Morocco and the adjacent shelf area using P-wave receiver functions, Geophysical Journal
417   International, 223(3), 1780-1793. doi:10.1093/gji/ggaa379

418   Revenaugh, J., and T. H. Jordan (1991), Mantle layering fromScSreverberations: 3. The upper mantle, Journal of
419   Geophysical Research: Solid Earth, 96(B12), 19781-19810. doi:10.1029/91jb01487
420   Schmerr, N. (2015), Imaging Mantle Heterogeneity with Upper Mantle Seismic Discontinuities, in The Earth's
421   Heterogeneous Mantle, edited, pp. 79-104.
422   Schmidt, M. W., and S. Poli (1998), Experimentally based water budgets for dehydrating slabs and consequences for
423   arc magma generation, Earth and Planetary Science Letters, 163(1-4), 361-379
424   Shinmei, T., N. Tomioka, K. Fujino, K. Kuroda, and T. Irifune (1999), In situ X-ray diffraction study of enstatite up
425   to 12 GPa and 1473 K and equations of state, American Mineralogist, 84(10), 1588-1594. doi:10.2138/am-1999-
426   1012
427   Shukla, G., Z. Q. Wu, H. Hsu, A. Floris, M. Cococcioni, and R. M. Wentzcovitch (2015), Thermoelasticity of Fe2+-
428   bearing bridgmanite, Geophysical Research Letters, 42(6), 1741-1749. doi:10.1002/2014gl062888
429   Sobolev, A. V., A. W. Hofmann, S. V. Sobolev, and I. K. Nikogosian (2005), An olivine-free mantle source of
430   Hawaiian shield basalts, Nature, 434(7033), 590-597. doi:10.1038/nature03411
431   Sobolev, A. V., et al. (2007), The amount of recycled crust in sources of mantle-derived melts, Science, 316(5823),
432   412-417. doi:10.1126/science. 1138113
433   Spieker, K., I. Wölbern, C. Thomas, M. Harnafi, and L. El Moudnib (2014), Crustal and upper-mantle structure
434   beneath the western Atlas Mountains in SW Morocco derived from receiver functions, Geophysical Journal
435   International, 198(3), 1474-1485. doi:10.1093/gji/ggu216
436   Srinu, U., P. Kumar, C. Haldar, M. R. Kumar, D. Srinagesh, and B. Illa (2021), X‐Discontinuity Beneath the
437   Indian Shield—Evidence for Remnant Tethyan Oceanic Lithosphere in the Mantle, Journal of Geophysical
438   Research: Solid Earth, 126(8). doi:10.1029/2021jb021890
439   Trønnes, R. G. (2009), Structure, mineralogy and dynamics of the lowermost mantle, Mineralogy and Petrology,
440   99(3-4), 243-261. doi:10.1007/s00710-009-0068-z
441   Troullier, N., and J. L. Martins (1991), Efficient pseudopotentials for plane-wave calculations, Phys Rev B, 43(3),
442   1993-2006. doi:10.1103/PhysRevB.43.1993
443   Valdez, M. N., Z. Q. Wu, Y. G. Yu, J. Revenaugh, and R. M. Wentzcovitch (2012), Thermoelastic properties of
444   ringwoodite (Fex,Mg1-x)2SiO4: Its relationship to the 520 km seismic discontinuity, Earth and Planetary Science
445   Letters, 351, 115-122. doi:10.1016/j.epsl.2012.07.024
446   Wang, W., and Z. Wu (2018), Elasticity of Corundum at High Pressures and Temperatures: Implications for Pyrope
447   Decomposition and Al-Content Effect on Elastic Properties of Bridgmanite, Journal of Geophysical Research:
448   Solid Earth, 123(2), 1201-1216. doi:10.1002/2017jb015088
449   Wentzcovitch, R. M. (1991), Invariant molecular-dynamics approach to structural phase transitions, Phys Rev B,
450   44(5), 2358-2361. doi:10.1103/PhysRevB.44.2358
451   Williams, Q., and J. Revenaugh (2005), Ancient subduction, mantle eclogite, and the 300 km seismic discontinuity,
452   Geology, 33(1). doi:10.1130/g20968.1
453   Woodland, A., C. McCammon, and R. Angel (1997), Intersite partitioning of Mg and Fe in Ca-free high-pressure
454   C2/c clinopyroxene, American Mineralogist, 82(9-10), 923-930
455   Woodland, A. B. (1998), The orthorhombic to high-Pmonoclinic phase transition in Mg-Fe Pyroxenes: Can it
456   produce a seismic discontinuity?, Geophysical Research Letters, 25(8), 1241-1244. doi:10.1029/98gl00857
457   Woodland, A. B., and R. J. Angel (1997), Reversal of the orthoferrosilite-high-P clinoferrosilite transition, a phase
458   diagram for FeSiO3 and implications for the mineralogy of the Earth's upper mantle, European Journal of
459   Mineralogy, 245-254
460   Woodland, A. B., C. McCammon, and R. J. Angel (1997), Intersite partitioning of Mg and Fe in Ca-free high-
461   pressure C2/c clinopyroxene, American Mineralogist, 82(9-10), 923-930. doi:10.2138/am-1997-9-1009
462   Wu, Z. Q., and R. M. Wentzcovitch (2011), Quasiharmonic thermal elasticity of crystals: An analytical approach,
463   Phys Rev B, 83(18). doi:10.1103/PhysRevB.83.184115
464   Wu, Z. Q., J. F. Justo, and R. M. Wentzcovitch (2013), Elastic anomalies in a spin-crossover system: ferropericlase
465   at lower mantle conditions, Phys Rev Lett, 110(22), 228501. doi:10.1103/PhysRevLett.110.228501
466   Yang, D. P., W. Z. Wang, and Z. Q. Wu (2017), Elasticity of superhydrous phase B at the mantle temperatures and
467   pressures: Implications for 800 km discontinuity and water flow into the lower mantle, Journal of Geophysical
468   Research-Solid Earth, 122(7), 5026-5037. doi:10.1002/2017jb014319
469   Yang, R., and Z. Wu (2014), Elastic properties of stishovite and the CaCl2-type silica at the mantle temperature and
470   pressure: An ab initio investigation, Earth and Planetary Science Letters, 404, 14-
471   21. doi:10.1016/j.epsl.2014.07.020

472 Yao, C., Z. Q. Wu, F. Zou, and W. D. Sun (2018), Thermodynamic and Elastic Properties of Magnesite at Mantle
473 Conditions: First-Principles Calculations, Geochemistry Geophysics Geosystems, 19(8), 2719-
474 2731. doi:10.1029/2017gc007396
475 Yasuda, A., T. Fujii, and K. Kurita (1994), Melting phase relations of an anhydrous mid-ocean ridge basalt from 3 to
476 20 GPa: Implications for the behavior of subducted oceanic crust in the mantle, Journal of Geophysical Research:
477 Solid Earth, 99(B5), 9401-9414. doi:10.1029/93jb03205
478 Yaxley, G. M., and D. H. Green (1998), Reactions between eclogite and peridotite: Mantle refertilisation by
479 subduction of oceanic crust, Schweizerische Mineralogische Und Petrographische Mitteilungen, 78(2), 243-255
480 Yu, Y. G., and R. M. Wentzcovitch (2009), Low-pressure clino- to high-pressure clinoenstatite phase transition: A
481 phonon-related mechanism, American Mineralogist, 94(4), 461-466. doi:10.2138/am.2009.3071
482 Zou, F., Z. Wu, W. Wang, and R. M. Wentzcovitch (2018), An Extended Semianalytical Approach for
483 Thermoelasticity of Monoclinic Crystals: Application to Diopside, Journal of Geophysical Research: Solid Earth,
484 123(9), 7629-7643. doi:10.1029/2018jb016102
485

Wide distribution and partial melting of eclogite indicated by the X-discontinuity in the upper mantle

Jian Song[1], Wangsheng Qian[1], Shangqin Hao[1], Wenzhong Wang[1,2,3], Daoyuan Sun[1,4], Zhongqing Wu[1,4,5*]

[1] Laboratory of Seismology and Physics of Earth's Interior, School of Earth and Space Sciences, University of Science and Technology of China, Hefei 230026, China.

[2] Department of Earth Sciences, University College London, London WC1E 6BT, United Kingdom.

[3] Earth and Planets Laboratory, Carnegie Institution for Science, Washington, DC 20015, USA.

[4] CAS Center for Excellence in Comparative Planetology, University of Science and Technology of China, Hefei, Anhui, China.

[5] National Geophysical Observatory at Mengcheng, Anhui, China.

Contents of this file

Introduction

The following supplementary materials provide first-principle calculation results of EOS of high-pressure clinoenstatite (HPCEN, $MgSiO_3$) together with previous experimental results (Table S1-S2), elastic constants of HPCEN (Figure S1, Table S3), the pressure and temperature dependency of elastic properties of HPCEN (Table S4).
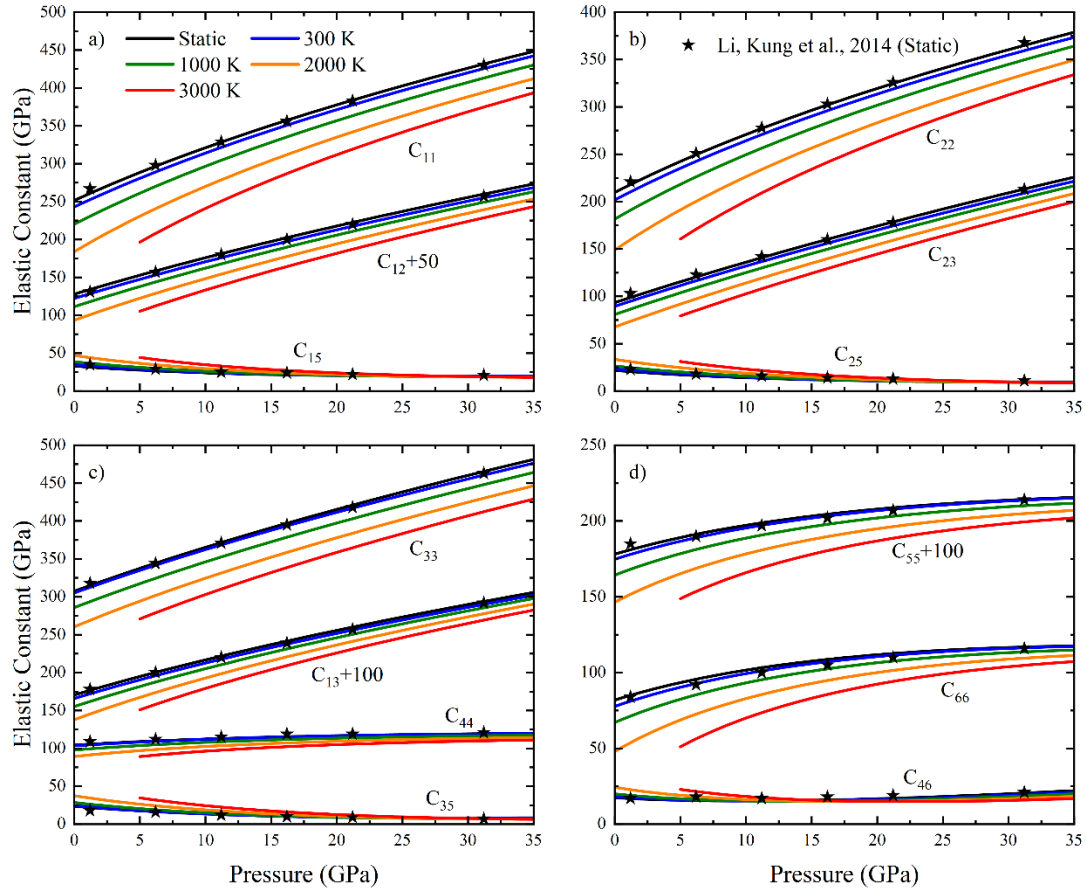
Figure S1. Elastic constants of HPCEN as a function of pressure at different temperature, in contrast to static GGA results of *Li et al.* (2014).

P (GPa)	T (K)	V (Å^3)	
		Shinmei et al. (1999)	This study
6.61	1173	392.4	393.3
7.32	300	381.9	383.7
8.69	300	378.5	380.3
9.20	300	377.0	379.2
10.68	300	373.8	375.9
11.22	573	374.2	376.8
11.27	873	376.3	379.3
9.23	300	376.9	379.2
9.04	300	377.6	379.4
10.19	573	376.4	378.9
11.35	873	376.1	379.2
11.75	1073	376.2	379.9
11.92	1273	378.2	381.7
11.14	1473	382.8	384.8
7.11	300	382.2	383.7
7.01	300	382.9	383.7
6.80	300	383.9	384.9
6.04	300	385.5	386.1
5.26	300	387.4	388.6
4.02	300	391.2	391.2
5.03	300	388.6	388.6
6.52	573	386.3	387.1
8.12	873	384.5	386.2
8.73	1173	385.5	388.0

Table S1. The volume of HPCEN at high pressure and high temperature.

	V_0 (Å^3)	K_{T0} (GPa)	K'_{T0}	
This study	402.4	127.4	5.25	
Lazarz et al. (2019)	401.2	129	4 (fixed)	
Lazarz et al. (2019) [a]	403.9	121	4 (fixed)	0 GPa, 300 K
Jacobsen et al. (2010)	404	119	6.1	
Shinmei et al. (1999)	405	106	5	
This study	384.5	160.6	5	6.5 GPa, 300 K
Kung et al. (2005)	385	155	5.5	

[a]. *Lazarz et al.* (2019) combined their results with those of *Angel and Hugh-Jones* (1994) together to fit the Birth-Murnaghan Equation with fixed K'_{T0}.

Table S2. Volume, isothermal bulk modulus and its derivative to pressure of HPCEN at 300 K.

P (GPa)	C_{11}	C_{22}	C_{33}	C_{12}	C_{13}	C_{23}	C_{44}	C_{55}	C_{66}	C_{15}	C_{25}	C_{35}	C_{46}
	Li et al. (2014) / This study												
1.2	267/261	221/218	318/315	109/106	85/81	84/85	81/84	78/77	103/99	35/32	23/21	18/22	17/17
6.2	298/297	251/250	344/344	112/110	90/91	96/92	107/109	100/100	123/120	29/27	18/16	16/16	18/16
11.2	329/328	278/277	372/371	115/113	97/99	103/100	131/130	120/122	142/141	25/23	16/14	12/13	17/15
16.2	356/357	303/302	395/397	119/115	102/104	105/109	150/152	139/142	160/160	24/21	12/14	10/10	18/16
21.2	383/384	326/325	418/421	119/117	107/109	110/113	170/173	157/160	178/179	22/20	13/10	9/9	19/17
31.2	430/432	365/368	463/465	121/119	114/114	117/116	207/210	192/194	213/213	21/20	11/10	8/7	21/21

Table S3. Elastic Constants (GPa) of HPCEN at static conditions. Both GGA results of *Li et al.* (2014) after pressure correction and LDA results of this study are listed.

Parameters	K_S	G	Parameters	V_P	V_S
M_0 (GPa)	126.7	82.73	M_0 ($km\ s^{-1}$)	8.452	4.995
$\dfrac{\partial M}{\partial P}$	6.425	2.042	$\dfrac{\partial M}{\partial P}$ ($km\ s^{-1}\ GPa^{-1}$)	0.128	0.0424
$\dfrac{\partial M}{\partial T}$ (MPa/K)	-21.38	-11.17	$\dfrac{\partial M}{\partial T}$ ($\times 10^{-3}\ km\ s^{-1}\ K^{-1}$)	-0.525	-0.266
$\dfrac{\partial^2 M}{\partial P^2}$ ($\times 10^{-3}\ GPa^{-1}$)	-68.89	-44.04	$\dfrac{\partial^2 M}{\partial P^2}$ ($\times 10^{-3}\ km\ s^{-1}\ GPa^{-2}$)	-2.659	-1.273
$\dfrac{\partial^2 M}{\partial P \partial T}$ ($\times 10^{-3}\ K^{-1}$)	0.5886	0.3755	$\dfrac{\partial^2 M}{\partial P \partial T}$ ($\times 10^{-6}\ km\ s^{-1}\ GPa^{-1}K^{-1}$)	23.56	12.08
$\dfrac{\partial^2 M}{\partial T^2}$ ($\times 10^{-6}\ GPa\ K^{-1}$)	-1.932	-0.088	$\dfrac{\partial^2 M}{\partial T^2}$ ($\times 10^{-6}\ km\ s^{-1}\ K^{-2}$)	-0.070	-0.032

Table S4. Elastic moduli and velocities of HPCEN and their first and second derivatives with respect to pressure and temperature. The polynomial fitting equation is $M = M_0 + \left(\frac{\partial M}{\partial P}\right) \cdot P + \left(\frac{\partial M}{\partial T}\right) \cdot (T - 300) + \left(\frac{\partial^2 M}{\partial P^2}\right) \cdot P^2 + \left(\frac{\partial^2 M}{\partial T^2}\right) \cdot (T - 300)^2 + \left(\frac{\partial^2 M}{\partial P \partial T}\right) \cdot P \cdot (T - 300), M = K_S, G, V_P, and\ V_S$. The fitting range is 0-25 GPa and 300-2000 K for pressure and temperature, respectively.